CrossMark

J. Fluid Mech. (2016), *vol.* 789, *pp.* 567–588. © Cambridge University Press 2016
doi:10.1017/jfm.2015.744

Amplitude modulation of streamwise velocity fluctuations in the roughness sublayer: evidence from large-eddy simulations

William Anderson†

Department of Mechanical Engineering, The University of Texas at Dallas, Richardson, TX, USA

(Received 5 August 2015; revised 2 December 2015; accepted 12 December 2015; first published online 26 January 2016)

Recent studies have demonstrated that large- and very-large-scale motions in the logarithmic region of turbulent boundary layers 'amplitude modulate' dynamics of the near-wall region (Marusic *et al.*, *Science*, vol. 329, 2010, pp. 193–196; Mathis *et al.*, *J. Fluid Mech.*, vol. 628, 2009*a*, pp. 311–337). These contributions prompted development of a predictive model for near-wall dynamics (Mathis *et al.*, *J. Fluid Mech.*, vol. 681, 2011, pp. 537–566) that has promising implications for large-eddy simulations of wall turbulence at high Reynolds numbers (owing to the presence of smaller scales as the wall is approached). Existing studies on the existence of amplitude modulation in wall-bounded turbulence have addressed smooth-wall flows, though high Reynolds number rough-wall flows are ubiquitous. Under such conditions, the production of element-scale vortices ablates the viscous wall region and a new near-wall layer emerges: the roughness sublayer. The roughness sublayer depth scales with aggregate roughness element height, h, and is typically $2h \sim 3h$. Above the roughness sublayer, Townsend's hypothesis dictates that turbulence in the logarithmic layer is unaffected by the roughness sublayer (beyond its role in setting the friction velocity and thus inducing a deficit in the mean streamwise velocity known as the roughness function). Here, we present large-eddy simulation results of turbulent channel flow over rough walls. We follow the decoupling procedure outlined in Mathis *et al.* (*J. Fluid Mech.*, vol. 628, 2009*a*, 311–337) and present evidence that outer-layer dynamics amplitude modulate the roughness sublayer. Below the roughness element height, we report enormous sensitivity to the streamwise–spanwise position at which flow statistics are measured, owing to spatial heterogeneities in the roughness sublayer imparted by roughness elements. For $y/h \gtrsim 1.5$ (i.e. above the cubes, but within the roughness sublayer), topography dependence rapidly declines.

Key words: atmospheric flows, turbulence modelling, turbulent flows

1. Introduction and background

High Reynolds number rough-wall turbulence is ubiquitous in engineering and geophysical flows (pipes, channels, and boundary layers) (Raupach, Antonia & Rajagopalan 1991; Jimenez 2004; Castro 2007; Flack & Schultz 2010). The

† Email address for correspondence: wca140030@utdallas.edu

https://doi.org/10.1017/jfm.2015.744 Published online by Cambridge University Press

momentum exchange between such flows and the bounding surface is critical to the performance of vapour power systems (Bons *et al.* 2001) and naval architecture surfaces on which growth of biological mass has occurred (Schultz 2007); environmental flow problems of interest include surface fluxes of momentum and scalars (temperature and humidity) associated with atmospheric boundary layer flows over complex natural landscapes (Bou-Zeid, Meneveau & Parlange 2005; Anderson & Meneveau 2011), urban environments (Bohm, Finnigan & Raupach 2000; Cheng & Castro 2002; Coceal *et al.* 2007; Harmon & Finnigan 2007; Xie, Coceal & Castro 2008; Belcher, Harman & Finnigan 2012; Anderson, Li & Bou-Zeid 2015), vegetative canopies (Chester, Meneveau & Parlange 2007; Finnigan, Shaw & Patton 2009; Bai, Meneveau & Katz 2012; Belcher *et al.* 2012; Graham & Meneveau 2012; Bailey & Stoll 2013), and distributions of wind turbines (Calaf, Meneveau & Meyers 2010; Calaf, Parlange & Meneveau 2011). Roughness ablates the viscous wall region – leaving in its place the so-called roughness sublayer – and induces a momentum deficit of the outer flow known as the roughness function, ΔU^+. Turbulence within the roughness sublayer is characterized by coherent structures with geometric macroscale on the order of individual roughness element height, h (Castro 2007). The roughness sublayer depth, y_{RSL}, scales linearly with h, and a consensus range is generally $2 \lesssim y_{RSL}/h \lesssim 5$ (Grass 1971; Raupach *et al.* 1991; Mejia-Alvarez & Christensen 2010). In the inertial sublayer above this, however, provided $\delta/h \gtrsim 40$ (where δ is the boundary layer thickness), Townsend's hypothesis states that a scale separation exists in which the outer-layer flow exhibits a universality independent of the roughness sublayer (with the exception of its response to the friction velocity, u_τ, and δ; Townsend 1976; Jimenez 2004). This has been largely confirmed by experiments, which demonstrate outer-layer similarity in the dynamical (hairpin vortex packets encapsulating low-momentum regions; Ganapathisubramani, Longmire & Marusic 2003; Hutchins & Marusic 2007*a*; Volino, Schultz & Flack 2007; Hong *et al.* 2012) and structural (two-point correlations; Wu & Christensen 2007, 2010) properties of smooth- and rough-wall turbulence. However, one notes the more recent experimental evidence from Hong *et al.* (2012), who showed that outer-layer streamwise velocity fluctuations displayed roughness influences in flow over topography composed of right square pyramids distributed such that the bases of neighbouring pyramids were in contact.

Numerical simulation of wall turbulence at high Reynolds number presents significant computational challenges. Turbulent kinetic energy production, $\mathscr{P} = \langle \boldsymbol{u}' \otimes \boldsymbol{u}' \rangle_T : \boldsymbol{\nabla} \langle \boldsymbol{u} \rangle_T$, where $\boldsymbol{u}$ is velocity, $\langle \cdot \rangle_T$ denotes time average, $\boldsymbol{u}' = \boldsymbol{u} - \langle \boldsymbol{u} \rangle_T$, and $\langle \boldsymbol{u}' \otimes \boldsymbol{u}' \rangle_T$ is the total (Reynolds) stress tensor, exhibits its maximum value in the roughness sublayer (Hong, Katz & Schultz 2011), and this is where the greatest burden on computational resolution is placed. Consider a computational domain with streamwise, spanwise, and wall-normal resolutions, N_x, N_y, and N_z, respectively, to be used for direct numerical simulation (DNS) of wall turbulence. (Note that in this document, $\boldsymbol{x} = \{x, y, z\}$ corresponds with the streamwise, wall-normal, and spanwise directions, respectively; $\boldsymbol{u} = \{u, v, w\}$ corresponds with the streamwise, wall-normal, and spanwise velocities, respectively.) The resolution requirement for this domain scales with Reynolds number as $N_x N_y N_z \sim Re_L^{9/4}$ (Piomelli & Balaras 2002; Piomelli 2008), where $Re_L = L u'_{rms}/\nu$ is the turbulent Reynolds number, L is the integral length scale of the flow, u'_{rms} is the root-mean-square of the fluctuating velocity, and ν is kinematic viscosity. This scaling demonstrates the practical limitations on DNS with increasing Re_L, and one notes that DNS of rough-wall flows are typically $Re_\tau = u_\tau \delta/\nu \lesssim 10^3$ (channel flows: Coceal *et al.*

https://doi.org/10.1017/jfm.2015.744 Published online by Cambridge University Press

2007; Leonardi & Castro 2010; Yuan & Piomelli 2014; pipe flow: Chan *et al.* 2015). For boundary layer flow over a roughness (i.e. $\delta/h \gtrsim 40$, Jimenez 2004), and presuming validity of Townsend's hypothesis (Wu & Christensen 2007, 2010), one notes that $Re_\tau \lesssim 1000$ would not capture the observed 'outer peak' in the logarithmic region (most readily discerned from premultiplied energy spectra of fluctuating streamwise velocity, u'; Hutchins & Marusic 2007*a*,*b*; Mathis, Hutchins & Marusic 2009*a*; Marusic, Mathis & Hutchins 2010; Mathis, Hutchins & Marusic 2011). According to Hutchins & Marusic (2007*a*), $Re_\tau \approx 2000$ is the 'threshold' for emergence of the outer peak, wherein meandering large- and very-large-scale motions (LSMs and VLSMs) are responsible for the observed spectral content in the logarithmic region. Flows in the atmospheric surface layer exhibit $Re_\tau \sim O(10^6)$ (Mathis *et al.* 2009*a*), which prompted the onset of large-eddy simulation (LES) (Deardorff 1970; Moeng 1984) as a means to resolve the largest scales of high Reynolds number flows while modelling the effects of small subgrid-scale motions (Mason 1994; Meneveau & Katz 2000).

Numerical prescription of rough-wall boundary conditions (as streamwise- and spanwise-wall-normal stresses, τ_{xy}^w and τ_{zy}^w, respectively) in high Reynolds number LES can be treated with varying techniques (Piomelli & Balaras 2002; Piomelli 2008). Equilibrium wall models (Pope 2000) set the surface stress at the first wall-normal computational grid point (Piomelli 2008) based on the associated flow conditions (more recent efforts have focused on generalizations of this approach; Yang *et al.* 2015). For flows over rough surfaces, wall models based on the equilibrium assumption are favourable since drag can readily be parameterized via a momentum roughness length, l (Anderson & Meneveau 2011), although *a priori* description of l based only on geometry of the roughness is itself an ongoing research effort (Flack & Schultz 2010). Note that the momentum roughness length is commonly called y_0 or z_0 (depending on coordinate system orientation), but we decided to use l here since y_0 is a commonly used symbol in the existing amplitude modulation literature. Alternatively, so-called zonal schemes account for inherent non-equilibrium in the near-wall region by solving a coupled set of equations (Balaras & Benocci 1994; Balaras, Benocci & Piomelli 1996), instead of assuming a constant-stress region. Hybrid schemes involve a Reynolds-averaged treatment in the near-wall region which integrates with an LES solver at a predefined wall-normal elevation (Sagaut 2002). It is beyond the scope of this document to fully review contemporary wall modelling approaches in LES. Suffice to say that treatment of the wall region is critical to advancing the predictive capabilities of LES.

Recent studies have demonstrated that LSMs and VLSMs in the logarithmic region of smooth-wall turbulent boundary layers, pipes, and channels 'amplitude modulate' dynamics of the near-wall region (Mathis *et al.* 2009*a*,*b*; Marusic *et al.* 2010); these findings build on the existing literature regarding an 'inner–outer' interaction in wall turbulence (Rao, Narasimha & Narayanan 1971; Bandyopadhyay & Hussain 1984). These contributions prompted development of a predictive model for dynamics of the inner layer, $u_p(x, y_i, z, t)$ (Mathis *et al.* 2011), based on attributes of flow in the outer layer, $u(x, y_O, z, t)$ (where u_p denotes predicted, y_i denotes an 'inner' elevation, and y_O denotes an 'outer' elevation). Such an approach has promising implications for LES of wall-bounded turbulence at high Reynolds numbers, in which the flow is well resolved – based on decomposition of x–y Reynolds shear stresses, $\langle u'v' \rangle = \langle \tilde{u}'\tilde{v}' \rangle + \langle \tau_{xy} \rangle$ – for $y_O/\delta \gtrsim 0.1$ (see figure 4 of Porté-Agel, Meneveau & Parlange 2000) but near-wall boundary conditions are plagued by a lack of resolution. Most existing studies

https://doi.org/10.1017/jfm.2015.744 Published online by Cambridge University Press

on the existence of amplitude modulation (AM) in wall-bounded turbulence have addressed smooth-wall flows and thus the viscous wall region; recently, Nadeem *et al.* (2015) used direct numerical simulation to determine the existence of an AM effect in turbulent boundary layer flow over a topography composed or spanwise bars, although one notes the inherent outer-layer differences in physics of wall turbulence responding to spanwise bars relative to three-dimensional roughness (Krogstad & Antonia 1994; Leonardi *et al.* 2003; Leonardi, Orlandi & Antonia 2007). Here, we explore the existence of AM in rough-wall flows (thus, AM of the roughness sublayer due to the passage of coherent structures in the outer inertial layer). We take this opportunity to note that the attributes of inclined meandering low- and high-momentum regions (LMRs and HMRs) have previously been considered as an input argument for equilibrium wall models of the inner layer (Piomelli *et al.* 1989; Marusic, Kunkel & Porté-Agel 2001).

1.1. *Amplitude modulation*

In the context of smooth-wall boundary layers, the AM 'decoupling procedure' is rigorously outlined in Mathis *et al.* (2009*a*). Here, we adopt this procedure under the assumption that the roughness sublayer is a structural analogue of the viscous wall region, thereby enabling y_i to be nominated as an elevation in the roughness sublayer (we have adopted $y_i/h \approx 1$, where y_i is referenced from the surface at which $y = 0$). Figure 1(*a*,*c*) shows perspective-style sketches of an array of uniform-height staggered cubes (Cheng & Castro 2002; Coceal *et al.* 2007) and a homogeneous roughness, respectively. In these figures, we have added annotations of y_i and y_O to demonstrate the inner and outer elevations, respectively (where $y_O/y_i > 1$, and y_O is above the roughness sublayer, i.e. $y_O/y_{RSL} > 1$). During LES, a time series of streamwise velocity is recorded over the domain depth (vertical red line in figure 1*a*,*c*), from which we can retrieve $\tilde{u}(x_l, y_i, z_l, t)/u_\tau$ and $\tilde{u}(x_l, y_O, z_l, t)/u_\tau$ (where subscript l denotes a local position in the wall-parallel plane, e.g. $\{x_1, z_1\}$ in figure 1(*b*) or $\{x_c, z_c\}$ in figure 1(*c*), and $\widetilde{\ldots}$ denotes a grid-filtered LES quantity). Hereafter, the inner and outer signals will be $\tilde{u}(y_i, t) = \tilde{u}(x_l, y_i, z_l, t)/u_\tau$ and $\tilde{u}(y_O, t) = \tilde{u}(x_l, y_O, z_l, t)/u_\tau$, for brevity. At each elevation, the time mean is subtracted:

$$\tilde{u}'(y, t) = \tilde{u}(y, t) - \langle \tilde{u}(y, t) \rangle_T. \tag{1.1}$$

In order to realize statistical stationarity for the present analysis, the simulations are run for $5 \times 10^3 \lesssim TU_0/\delta \lesssim 1 \times 10^4$ (Hutchins *et al.* 2009), where U_0 is the time-averaged centreline streamwise velocity. This rather long averaging time is needed to ensure that an adequately high number of LMRs and HMRs advect through the domain and thus are embodied in the resulting time series and flow statistics. Following Mathis *et al.* (2009*a*), $\tilde{u}'(y_i, t)$ and $\tilde{u}'(y_O, t)$ are low-pass filtered at scale δ, $\tilde{u}'_L(y_i, t) = G_\delta \star \tilde{u}'(y_i, t)$ and $\tilde{u}'_L(y_O, t) = G_\delta \star \tilde{u}'(y_O, t)$, respectively, where $\star$ denotes a convolution. We used a sharp spectral filter: $G_\delta(\boldsymbol{x}) = \Pi \sin(\pi \boldsymbol{x}/\delta)/(\pi \boldsymbol{x})$ (i.e. filtering at one eddy turnover) (Meneveau & Katz 2000; Pope 2000); the choice of filter is not expected to substantially influence the resulting statistics. Application of the filter enables extraction of the small (sub-δ) inner velocity fluctuations, $\tilde{u}'_S(y_i, t) = \tilde{u}'(y_i, t) - \tilde{u}'_L(y_i, t)$, which are of primary interest for characterizing Reynolds-stress-producing processes. Note, however, that $\tilde{u}'_S(y_i, t)$ is a spatially resolved quantity since $\delta/\Delta > 1$. Mathis *et al.* (2009*a*) demonstrated that the Hilbert transform can be used to determine the extent to which $\tilde{u}'_S(y_i, t)$ is amplitude modulated by $\tilde{u}'_L(y_O, t)$ (i.e. LMRs and HMRs in the outer layer that are

https://doi.org/10.1017/jfm.2015.744 Published online by Cambridge University Press

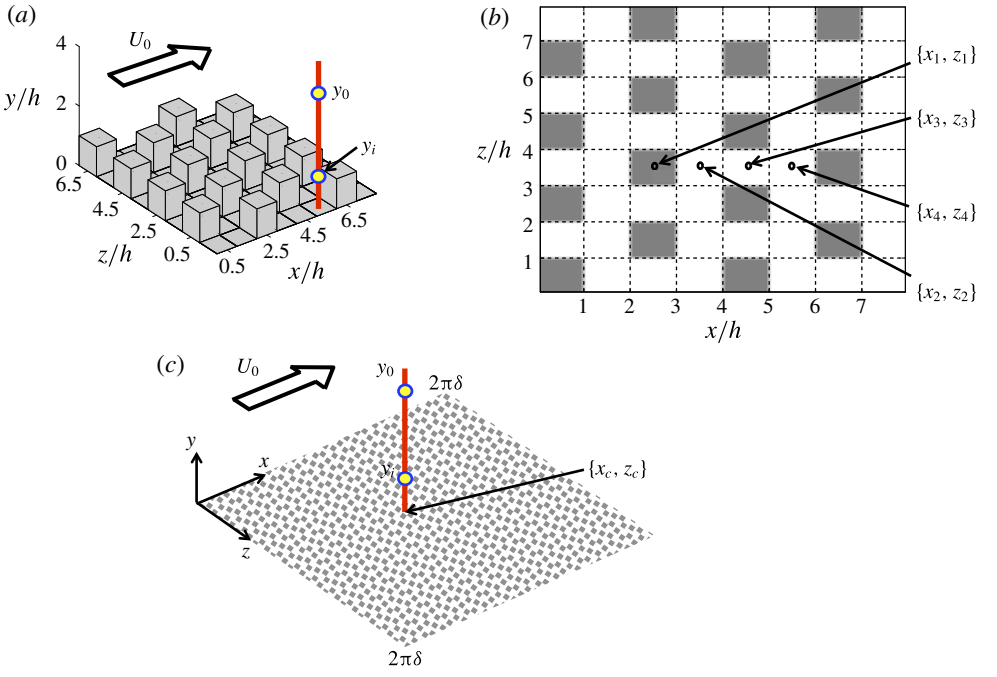


FIGURE 1. Illustration of cases considered as lower topographies for the present study. (*a*,*b*) Show the uniform-height staggered cube arrangement (considered also by Cheng & Castro (2002) and Coceal *et al.* (2007)), named case 'CR'. Panel (*a*) is a perspective image, while (*b*) is a planform image with indication of positions at which time–height velocity data are recorded. Owing to the topography attributes, the four points effectively capture temporal dynamics at all points in the domain. (*c*) Shows the homogeneous roughness case, named 'HR'. In (*a*,*c*), the free-stream flow direction, U_0, is shown. For illustration, examples of the inner, y_i, and outer, y_O, elevations are shown.

well resolved on the LES mesh). By computing the Hilbert transform of $\tilde{u}'_S(y_i,\ t)$, $\mathscr{H}(t)$, we can determine the complex analytic function, $Z(t) = \tilde{u}'_S(y_i,\ t) + \mathrm{i}\mathscr{H}(t) = A(t)\mathrm{e}^{\mathrm{i}\phi(t)}$, where $A(t)$ and $\phi(t)$ are modulus and phase, respectively. Here, $A(t)$ is the envelope of the original signal, termed here as $E(\tilde{u}'_S(y_i,\ t))$. The final step of the procedure involves low-pass filtering of the envelope, $E_L(\tilde{u}'_S(y_i,\ t)) = G_\delta \star E(\tilde{u}'_S(y_i,\ t))$, which quantifies the modulation of $\tilde{u}'_S(y_i,\ t)$ by large-scale well-resolved modes.

1.2. *Present study*

Here, we present results of large-eddy simulation of turbulent half-channel flow over rough walls. We follow the decoupling procedure outlined in Mathis *et al.* (2009*a*) and § 1.1, and present evidence that outer-layer dynamics amplitude modulate the roughness sublayer. We report enormous sensitivity to the streamwise–spanwise position at which flow statistics are measured, owing to spatial heterogeneities in the roughness sublayer imparted by roughness elements. Section 2 briefly summarizes the LES code and cases, results are presented in § 3, and concluding remarks are made in § 4.

https://doi.org/10.1017/jfm.2015.744 Published online by Cambridge University Press

Topography (description)	N	$\frac{L_x}{\delta}$	$\frac{L_z}{\delta}$	$\frac{U_0 T}{\nu}$	$\frac{l}{\delta}$	$\frac{\delta}{h}$	$\approx\frac{y_{RSL}}{\delta}$	$N_{x,C}$	$\frac{y_O}{\delta}$
HR (homogeneous z_0)	96 128	2π	2π	7500 4660	1×10^{-3}	1×10^{2}	0.02	— —	0.16
CR (staggered cubes)	64 96 128	2	2	6571 6367 5348	1×10^{-2}	4	0.5	8 12 16	0.60

TABLE 1. Summary of simulation attributes.

2. Large-eddy simulation and cases

The LES code integrates the three-dimensional momentum transport equations,

$$\frac{\partial\tilde{\boldsymbol{u}}}{\partial t}+\frac{1}{2}\boldsymbol{\nabla}(\tilde{\boldsymbol{u}}\cdot\tilde{\boldsymbol{u}})-\tilde{\boldsymbol{u}}\times\tilde{\boldsymbol{\omega}}=-\frac{1}{\rho}\boldsymbol{\nabla}\tilde{p}-\boldsymbol{\nabla}\cdot\boldsymbol{\tau}+\boldsymbol{\Pi}+\frac{1}{\rho}\boldsymbol{f}, \tag{2.1}$$

where $\boldsymbol{\tau}=\widetilde{\boldsymbol{u}\otimes\boldsymbol{u}}-\tilde{\boldsymbol{u}}\otimes\tilde{\boldsymbol{u}}$ is the subgrid-scale stress tensor and $\boldsymbol{\Pi}=\{u_\tau^2/\rho\delta=1,0,0\}$ is an imposed pressure-gradient forcing, where δ is (now) the channel half-height. The present LES code is frequently used to model the atmospheric boundary layer (where dimensional values of $u_\tau=0.45$ m s^{-1} and $\delta=1000$ m are used for the purpose of normalizing time), and thus viscous stresses are neglected owing to the 'fully rough' conditions (Stevens, Wilczek & Meneveau 2014). The code has been used for diverse research efforts (Albertson & Parlange 1999; Porté-Agel *et al.* 2000; Bou-Zeid *et al.* 2005; Chester *et al.* 2007; Calaf *et al.* 2010, 2011; Anderson & Meneveau 2011; Graham & Meneveau 2012; Anderson & Chamecki 2014; Stevens *et al.* 2014; Wilczek, Stevens & Meneveau 2015). A solenoidal velocity field is maintained by computing the divergence of (2.1), applying the incompressibility condition, $\boldsymbol{\nabla}\cdot\tilde{\boldsymbol{u}}=0$, and solving the resultant pressure Poisson equation with Neumann conditions at the domain top and bottom, $\partial\tilde{p}/\partial y|_{y/\delta=1}=0$ and $\partial\tilde{p}/\partial y|_{y/\delta=0}=0$, respectively. The deviatoric component of $\boldsymbol{\tau}$ is evaluated using the eddy viscosity modelling approach, $\boldsymbol{\tau}-(1/3)\boldsymbol{\delta}\,\mathrm{Tr}(\boldsymbol{\tau})=-2\nu_t\tilde{\boldsymbol{S}}$, where $\nu_t=(C_s\Delta)^2|\tilde{S}|$ is the turbulent viscosity, C_s is the Smagorinsky coefficient (Smagorinsky 1963), Δ is the filter size, $\tilde{\boldsymbol{S}}=(\boldsymbol{\nabla}\tilde{\boldsymbol{u}}+\boldsymbol{\nabla}\tilde{\boldsymbol{u}}^{\mathrm{T}})/2$ is the resolved strain-rate tensor, and $|\tilde{S}|=(2\tilde{\boldsymbol{S}}:\tilde{\boldsymbol{S}})^{1/2}$ is the magnitude of the resolved strain-rate tensor. The scale-dependent Lagrangian model of Bou-Zeid *et al.* (2005) is used to evaluate C_s. The code is run with $N_x=N_y=N_z=N$ grid points, as summarized in table 1. The large number of eddy turnovers needed to attain stationary flow statistics for the AM analysis – $5\times10^3\lesssim TU_0/\delta\lesssim1\times10^4$ (Hutchins *et al.* 2009) – made relatively coarse meshes appealing. Nonetheless, by varying N for the same cases we demonstrate resolution invariance (i.e. the coarse meshes are perfectly adequate for accomplishing the goals of this study).

Two topographies are considered: an array of uniform-height staggered cubes (CR) and a homogeneous roughness (HR). Figure 1 shows the topographies and the caption provides some accompanying comments about the annotations. For HR, the topographic height distribution is everywhere zero, $h(x,z)=0$, and aerodynamic drag is modelled only with an aerodynamic roughness length, $l/\delta=1\times10^{-3}$, via the equilibrium logarithmic law (Deardorff 1970; Piomelli & Balaras 2002):

$$\frac{\tau_{xy}^w(x,\Delta_y/2,z)}{\rho}=-\left[\frac{\kappa U(x,\Delta_y/2,z)}{\log(y/l)}\right]^2\frac{\widehat{\tilde{u}}(x,\Delta_y/2,z)}{U(x,\Delta_y/2,z)} \tag{2.2}$$

https://doi.org/10.1017/jfm.2015.744 Published online by Cambridge University Press

and

$$\frac{\tau_{zy}^{w}(x,\,\Delta_y/2,\,z)}{\rho} = -\left[\frac{\kappa U(x,\,\Delta_y/2,\,z)}{\log(y/l)}\right]^2 \frac{\widehat{\tilde{w}}(x,\,\Delta_y/2,\,z)}{U(x,\,\Delta_y/2,\,z)}, \tag{2.3}$$

where κ is the von Kármán constant ($\kappa = 0.4$), $\widetilde{\ldots}$ and $\widehat{\widetilde{\ldots}}$ denote grid- and test-filtered quantities, respectively, and $U(x,\,\Delta_y/2,\,z) = [\widehat{\tilde{u}}^2(x,\,\Delta_y/2,\,z) + \widehat{\tilde{w}}^2(x,\,\Delta_y/2,\,z)]^{1/2}$ is the magnitude of the local test-filtered velocity. We follow Bou-Zeid *et al.* (2005) by using the test-filtered velocities for computing the wall stress ((2.2) and (2.3)). This approach is typically used for modelling flows over heterogeneous (Bou-Zeid *et al.* 2005) or complex topographies (Anderson & Meneveau 2010), since it serves to reduce variance of the streamwise and spanwise velocity components close to the wall, thereby improving prediction of the logarithmic law. We prescribed an l/δ for case HR. For case CR (and reported in table 1), l/δ was determined *a posteriori* by fitting a logarithmic profile to the inertial layer profile and extrapolating for the zero-velocity intercept (Anderson *et al.* 2015). Of course, results for case HR lack the mixing layer-like structure exhibited by case CR (wherein cubes absorb momentum, induce vortex shedding, and result in an inflected mean streamwise velocity profile, Ghisalberti 2009). For case CR, we can assume that $y_{RSL}/\delta \approx 2h/\delta$ (although, as discussed further below, the streamwise velocity profiles all tend to the plane-averaged logarithmic trend below this). For case HR, we can estimate y_{RSL} using classical relations that relate statistical attributes of the topography to aerodynamic roughness length, for example (Garratt 1994):

$$\frac{l}{h} = \gamma_1\left(1 - \frac{d}{h}\right), \tag{2.4}$$

where d is the zero-place displacement, h is the canopy or element height, and $0.2 \lesssim \gamma_1 \lesssim 0.4$. For discussion, let us assume that the roughness element density is such that $d/h = 0.5$, thus indicating that $0.1 \lesssim l/h \lesssim 0.2$. For discussion, we further assume that $l/h = 0.1$, and therefore $y_{RSL}/\delta \approx 2h/\delta = 20l/\delta$ if we again assume that $y_{RSL} = 2h$ (where all lengths are in the wall-normal direction with origin at $y/\delta = 0$). These elevations become significant later when nominating inner and outer elevations such that $y_i/y_{RSL} < 1$ and $y_O/y_{RSL} > 1$, respectively (i.e. revealing the extent to which outer-layer flow features amplitude modulate the roughness sublayer). The values of y_{RSL}/δ for cases HR and CR are summarized in table 1. Note that velocity is scaled with a numerical shear velocity, evaluated as $u_\tau^2 = \max\langle\tilde{u}'\tilde{v}' + \tau_{xy}\rangle_{T,x,z}$, where $\tilde{\boldsymbol{u}}'$ was defined with (1.1), τ_{xy} is the streamwise–wall-normal component of the subgrid-scale stress tensor, and $\langle\cdot\rangle_{T,x,z}$ denotes time and planar averaging (Finnigan 2000; Calaf *et al.* 2010; Bailey & Stoll 2013). Thus, for case HR, $u_\tau^2 = \langle\tau_{xy}^{w}\rangle_{T,x,z}$ (2.2). However, for case CR, in which $\max\langle\tilde{u}'\tilde{v}' + \tau_{xy}\rangle_{T,x,z}$ occurs approximately at the cube height (Coceal *et al.* 2007; Ghisalberti 2009; Anderson *et al.* 2015), turbulent stresses associated with the resolved and subgrid scales must be considered.

The topography function, $h(x,\,z)$, for case CR exhibits two values – 1/4 and 0 – depending on if $\{x,\,z\}$ corresponds with the position of a cube or flat ground, respectively (see also figure 1*b* and table 1). Where $h(x,\,z) = 0$, the equilibrium logarithmic law with $l/\delta = 1 \times 10^{-4}$ is used ((2.2) and (2.3)); we emphasize that this l/δ is not the aforementioned 'effective' value that is reported in table 1. For $h(x,\,z)/\delta = 1/4$, the cubes protrude far into the computational domain, and the immersed boundary method (IBM) is used (Anderson & Meneveau 2010; Anderson 2012). Table 1 shows the number of streamwise computational points per cube across

https://doi.org/10.1017/jfm.2015.744 Published online by Cambridge University Press

resolutions, $N_{x,C} = (h/L_x)N_x$ (note that the number of spanwise points is equivalent). This number is consistent with some previous LES studies of flow over obstacles (Tseng, Meneveau & Parlange 2006); more recently, Graham & Meneveau (2012) cited $N_{x,C} = 8$ as a minimum for LES of flow over obstacles. We also show negligible resolution dependence in results of the present study. Use of the IBM appears as a body force, $\boldsymbol{f}$, in (2.1). The present IBM imposes aerodynamic drag based on spatial variation of $h(x, z)$. The present IBM is based on a wall model to prescribe momentum depletion at fluid cells peripheral to the solid surface (similar to Chester *et al.* 2007, and within the continuous forcing class of IBM techniques; Mittal & Iaccarino 2005). This differs from a direct (or discrete) forcing approach in which velocity at adjacent fluid cells is reconstructed (Mittal & Iaccarino 2005; Lundquist, Chow & Lundquist 2010) to an *a priori* defined order of accuracy. For regions where $h(x, z)/\delta = 1/4$ (i.e. exceeding height of the first $\tilde{u}$ and $\tilde{w}$ grid point in the vertically staggered computational mesh), the aerodynamic drag force imposed on the flow by $h(x, z)$ is

$$\boldsymbol{F} = -\int_S p^w \boldsymbol{n}\, \mathrm{d}S, \tag{2.5}$$

where $\boldsymbol{n}$ is the unit normal vector to $h(x, z)$ and p^w is the resolved wall pressure acting on $h(x, z)$. This IBM technique (previously named the gradient-based drag modelling technique) is used to model pressure drag forces due to p^w. After division by density, ρ, and local computational cell volume, $\Delta_x\Delta_y\Delta_z$, (2.5) reduces to a drag force per unit mass required in (2.1):

$$\frac{1}{\rho}\boldsymbol{f} = -\frac{1}{\rho\Delta^2\Delta_y}\int_S p^w \boldsymbol{n}\, \mathrm{d}S \approx -\tilde{\boldsymbol{u}} R(\tilde{\boldsymbol{u}} \cdot \boldsymbol{\nabla} h)\frac{1}{\Delta_y}, \tag{2.6}$$

where $R(x)$ is the ramp function ($R(x) = x$ if $x \geqslant 0$, and $R(x) = 0$ if $x < 0$) and $\boldsymbol{\nabla} h = \{\partial h/\partial x, \partial h/\partial z\}$ contains the horizontal gradients of $h(x, z)$. This use of the ramp function isolates frontal areas of $h(x, z)$ on which $\tilde{\boldsymbol{u}}$ impinges. The drag coefficient is set to $C_d = 2$ for all cases and therefore the typical $C_d/2$ prefactor is omitted in (2.6) (this implies complete depletion of incoming momentum under fully rough conditions, Jimenez 2004). The IBM approach has been tested against numerous datasets available in the literature for flow over different kinds of topography – blocks, sinusoids, and ellipsoidal mounds – and in all cases the performance was satisfactory (agreement of time- and plane-averaged streamwise velocity profiles within 10 %). Equation (2.6) models drag associated with 'cut' cells (Mittal & Iaccarino 2005; Chester *et al.* 2007; Lundquist *et al.* 2010; Graham & Meneveau 2012) while the velocity at fully immersed internal cells is set to zero. For comparison of the present IBM against the Cheng & Castro (2002) dataset, please see Anderson *et al.* (2015).

3. Results

To illustrate how the passage of coherent structures (LMRs and HMRs) in the outer layer affects processes in the roughness sublayer, we have first generated time–height contours of fluctuating streamwise velocity, $\tilde{u}'(y, t)$, for cases HR and CR (1.1). These plots are generated by recording time series of velocity across the depth of the domain (vertical red line in figure 1*a*,*c*) (Anderson *et al.* 2015). Thus, LES is used to attain datasets that would be more commonly associated with a micrometeorological field campaign, for example, where a series of sonic anemometers are mounted on a tower. Figure 2 shows contours of $\tilde{u}'(y, t)$ for cases HR (*a*) and CR (*b* and *c* correspond

https://doi.org/10.1017/jfm.2015.744 Published online by Cambridge University Press

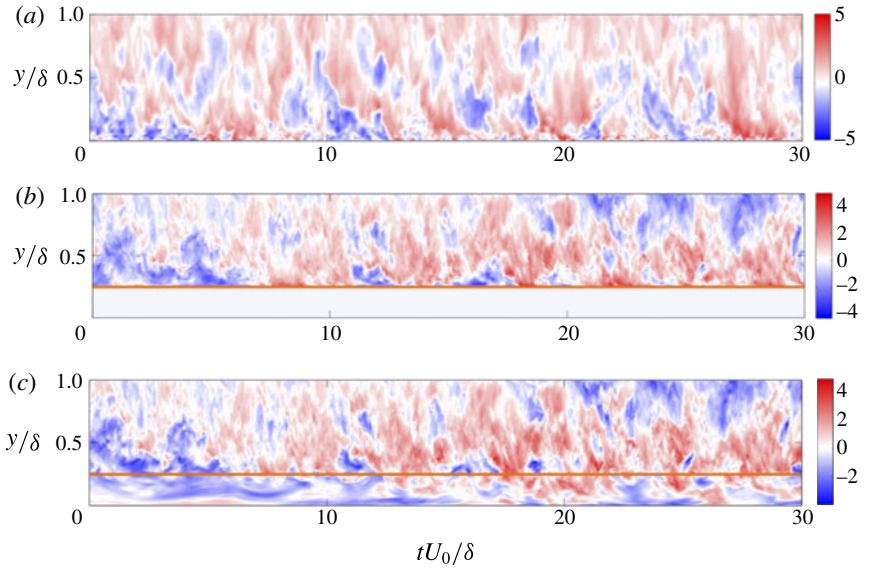


FIGURE 2. Time–height contours of fluctuating streamwise velocity, $\tilde{u}'(y,\ t)/u_\tau$, over $tU_0/\delta = 30$ eddy turnovers. Panel (*a*) is for HR at position $\{x_c, z_c\}$ in figure 1(*c*). Panel (*b*,*c*) are for CR at positions $\{x_1, z_1\}$ and $\{x_4, z_4\}$, respectively (please see figure 1*b* for reference). In (*b*,*c*), horizontal orange line denotes h/δ.

with time series at positions $\{x_1, z_1\}$ and $\{x_4, z_4\}$, respectively; see also figure 1*b*). Positions $\{x_1, z_1\}$ (figure 2*b*) and x_4 (figure 2*c*) were chosen for illustration given their positions above and immediately upwind of cubes (please see Anderson *et al.* (2015) for additional visualizations). In all cases, the $\tilde{u}'(y, t)$ contours exhibit a clear time lag between the passage of LMRs (HMRs) in the outer layer ($y/\delta \gtrsim 0.5$) and suppression (excitation) of activity in the roughness sublayer (Mathis *et al.* 2011). Consider, for example, the figure 2(*c*) contour in the interval $15 \lesssim tU_0/\delta \lesssim 18$. It is apparent that the magnitude of $\tilde{u}'$ fluctuations increases as the aloft HMR passes by. In an earlier study, we included contours of resolved Reynolds shear stresses (streamwise–wall-normal component: $\tilde{u}'\tilde{v}'$) owing to turbulent sweeps ($\tilde{u}' > 0$; $\tilde{v}' < 0$) and ejections ($\tilde{u}' < 0$; $\tilde{v}' > 0$) on figure 2-style $\tilde{u}'$ contours (Anderson *et al.* 2015). It was comprehensively shown that $\tilde{u}'\tilde{v}'$ owing to sweeps and ejections was always elevated following the passage of high- and low-momentum regions, respectively, and that the largest values occurred in the roughness sublayer. Consideration of the figure 2 contours thus provides some qualitative support for arguments that an underlying AM process takes place for the present high-Re_τ rough-wall channel flow cases. In Anderson *et al.* (2015), we compared local mean streamwise velocity profiles for case CR against literature and DNS results, and reported strong agreement.

To advance the discussion, we now present results of the AM decoupling procedure, as outlined in Mathis *et al.* (2009*a*) and briefly repeated in § 1.1. We have applied the decoupling procedure to time series for the HR and CR cases at elevations that capture the roughness sublayer ($y_i/y_{RSL} < 1$) and inertial layer ($y_O/y_{RSL} > 1$). For case HR, figure 3 shows time series of AM parameters at $y_i/\delta \approx 0.004$, based on the large-scale modulating signal at $y_O/\delta \approx 0.1$ (recall table 1, which shows that $y_i/\delta < y_{RSL}/\delta < y_O/\delta$). Figure 3(*a*) shows the small- and large-scale signals, $\tilde{u}'_S(y_i,\ t)$ and $\tilde{u}'_L(y_i,\ t)$. Added for illustration is grey shading where $\tilde{u}'_S(y_i,\ t)$ exhibits high

https://doi.org/10.1017/jfm.2015.744 Published online by Cambridge University Press

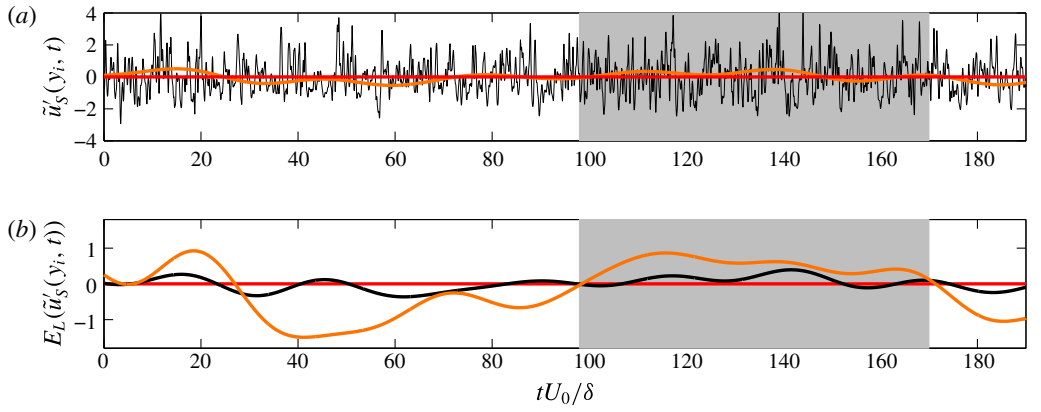


FIGURE 3. Time series of velocity and AM parameters (recall § 1.1 decomposition process) from LES of flow over figure 1(*c*) homogeneous roughness. (*a*) Shows low- and high-pass-filtered velocity, $\tilde{u}'_S(y_i, t)$ (black line) and $\tilde{u}'_L(y_i, t)$ (orange line), respectively, at inner location; (*b*) shows low-pass-filtered envelope of small-scale inner velocity, $E_L(\tilde{u}'_S(y_i, t))$ (black line), and time-shifted low-pass-filtered outer velocity, $\tilde{u}'_L(y_O, t + \delta\tau(y_O; y_i))$ (orange line). Grey shading is added for illustration of AM effects during passage of a coherent high-momentum region. For this figure, the inner and outer elevations are $y_i/\delta = 0.004$ and $y_O/\delta = 0.1$, respectively.

variance. It is clear that periods when $\tilde{u}'_S(y_i, t)$ varies dramatically correspond with $\tilde{u}'_L(y_i, t) > 0$. In contrast, during the interval $30 \lesssim tU_0/\delta \lesssim 100$, $\tilde{u}'_L(y_i, t) < 0$ and $\tilde{u}'_S(y_i, t)$ is relatively quiescent. Following Mathis *et al.* (2009*a*), we show the low-pass-filtered envelope, $E_L(\tilde{u}'_S(y_i, t))$, in figure 3(*b*). Here, $E_L(\tilde{u}'_S(y_i, t))$ is important, since it is absent in small-scale effects in the 'carrier' and illustrates only the influence of larger-scale inertial layer flow structures. To objectively demonstrate this, figure 3(*b*) shows $E_L(\tilde{u}'_S(y_i, t))$ and $\tilde{u}'_L(y_O, t + \delta\tau(y_O; y_i))$, where the $\delta\tau(y_O; y_i)$ correction accounts for the advective lag evident in figure 2. Recently, Anderson *et al.* (2015) showed that a shear-normalized advective lag ($u_\tau\delta^{-1}$; Stevens *et al.* 2014) can be determined *a priori* using canonical attributes of coherent structures in the flow. If an advective velocity, U_0, and streamwise correlation length, L_s, are known, these can be combined to determine the time before a uniform momentum parcel of fluid will advect past a sampling point. The logarithmic law and inclination angle are thus introduced:

$$\frac{U_0}{u_\tau} = \frac{1}{\kappa}\log\left(\frac{\delta}{l}\right) \quad \text{and} \quad L_s = \frac{y_0 - y}{\tan(\gamma)}, \tag{3.1a,b}$$

where $\kappa = 0.4$ is the von Kármán constant ($\kappa = 0.4$), l is the aerodynamic roughness length, and γ is the inclination angle of coherent structures ($\gamma = 15°$) (Coceal *et al.* 2007; Hong *et al.* 2011, 2012). Dividing length by advective velocity and applying the shear normalization factor, $u_\tau\delta^{-1}$, yields an advective lag:

$$\delta\tau(y; y_O)u_\tau\delta^{-1} = \frac{\kappa(y_O - y)}{\tan(\gamma)\delta\log(\delta/l)}. \tag{3.2}$$

Equation (3.2) predictions compared favourably against the actual advective lag, based on computation of the correlation between fluctuating streamwise velocity at different

https://doi.org/10.1017/jfm.2015.744 Published online by Cambridge University Press

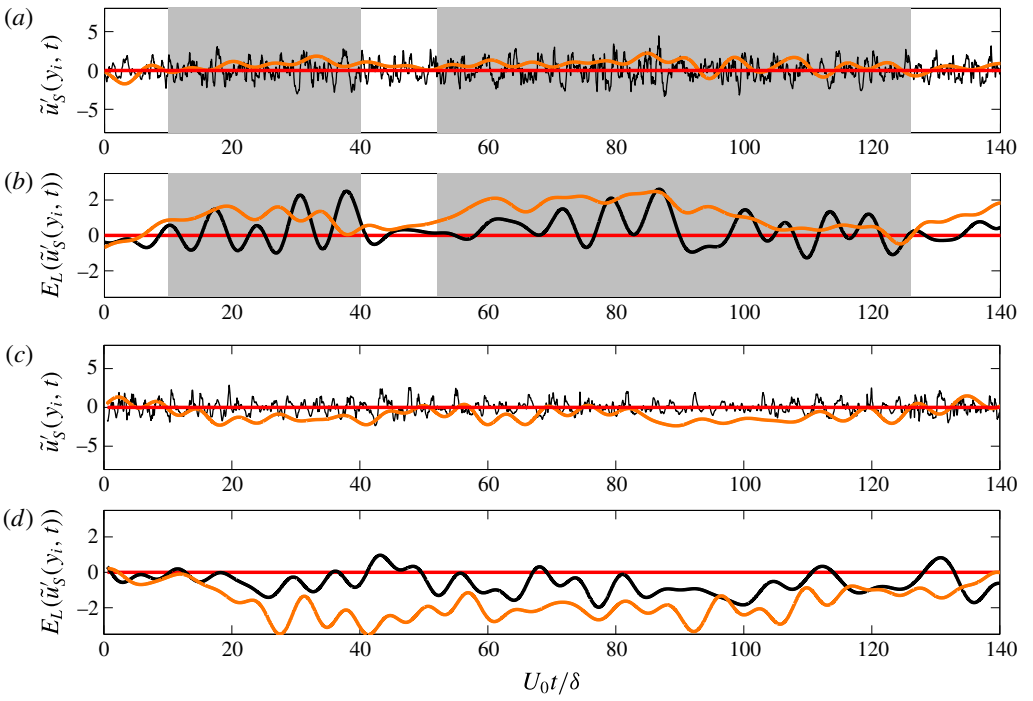


FIGURE 4. Time series of velocity and AM parameters (recall § 1.1 decomposition process) from LES of flow over figure 1(*a*) cubic topography, at position $\{x_4, z_4\}$ in figure 1(*b*). (*a*,*c*) Show low- and high-pass-filtered velocity, $\tilde{u}'_S(y_i, t)$ (black line) and $\tilde{u}'_L(y_i, t)$ (orange line), respectively, at inner location; (*b*,*d*) show low-pass-filtered envelope of small-scale inner velocity, $E_L(\tilde{u}'_S(y_i, t))$ (black line), and time-shifted low-pass-filtered outer velocity, $\tilde{u}'_L(y_O, t + \delta\tau(y_O; y_i))$ (orange line). In (*a*,*b*), grey shading is added for illustration of AM effects during passage of a coherent high-momentum region. For this figure, the inner and outer elevations are $y_i/\delta = 0.254$ and $y_O/\delta = 0.5$, respectively.

elevations. For all subsequent applications of the (3.2) time lag, we remove the $u_\tau\delta^{-1}$ normalization factor; note also that time, t, is normalized by $u_\tau\delta^{-1}$ when combined with $\delta\tau$. Figure 3 illustrates that the passage of LMRs ($\tilde{u}'_L(y_O, t + \delta\tau(y_O; y_i)) < 0$) and HMRs ($\tilde{u}'_L(y_O, t + \delta\tau(y_O; y_i)) > 0$) in the inertial layer corresponds closely with the inner-layer modulation of small scales as evidenced by $E_L(\tilde{u}_S(y_i, t)) < 0$ and $E_L(\tilde{u}_S(y_i, t)) > 0$, respectively.

For flow over case CR, figure 4 shows results of the AM decoupling procedure at position $\{x_4, z_4\}$ (see figure 1 for a schematic). The results are entirely consistent with those for case HR (figure 3). During the passage of a HMR (i.e. figure 4*a*,*b*: $5 \lesssim tU_0/\delta \lesssim 40$ and $50 \lesssim tU_0/\delta \lesssim 125$), the envelope of the small-scale inner velocity illustrates a clear modulation by the inertial layer velocity. Likewise, during quiescent periods when LMRs pass through the domain (figure 4*c*,*d*), there is also convincing evidence that $E_L(\tilde{u}'_S(y_i, t))$ is modulated by $\tilde{u}'_L(y_O, t + \delta\tau(y_O; y_i)) > 0$. For brevity, similarly formatted figures for positions x_2 and x_3 have been excluded here, although they portray the same relations. We emphasize that $\tilde{u}'_L(y_O, t)$ would be well resolved – based on decomposition of x–y Reynolds shear stresses, $\langle u'v' \rangle = \langle \tilde{u}'\tilde{v}' \rangle + \langle \tau_{xy} \rangle$ – for $y_O/\delta \gtrsim 0.1$ during LES (see, for example, figure 4 of Porté-Agel *et al.* (2000), figure 4 of Bou-Zeid *et al.* (2005), or figure 14 of Anderson & Meneveau (2011)).

https://doi.org/10.1017/jfm.2015.744 Published online by Cambridge University Press

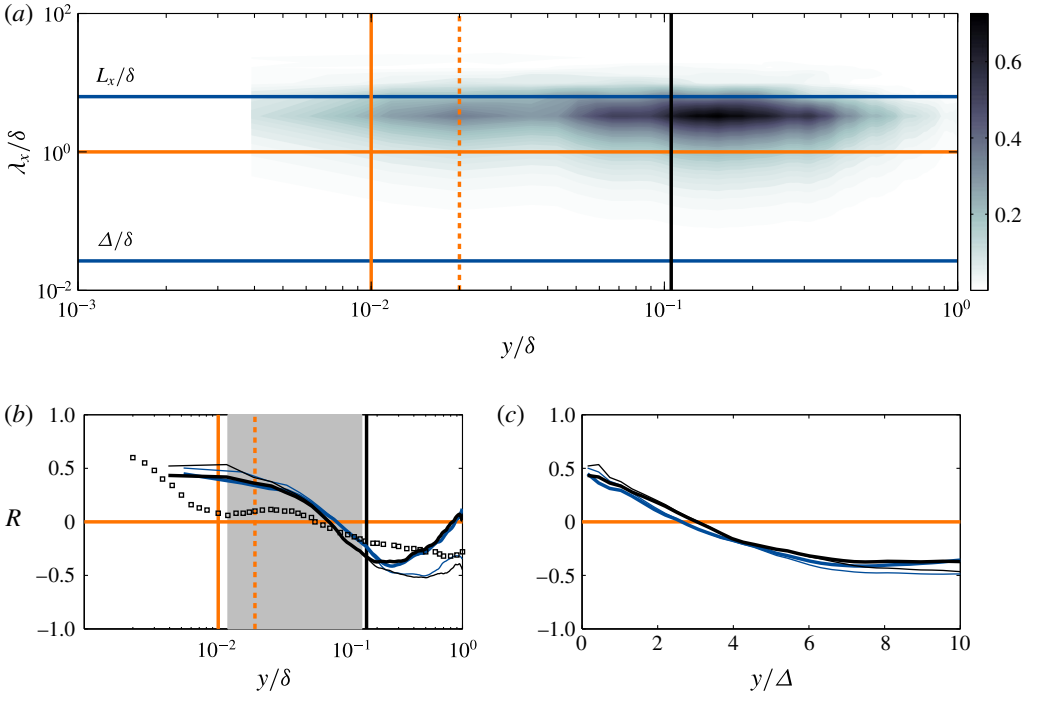


FIGURE 5. Statistics for flow over case HR. (*a*) Shows premultiplied spectral density of streamwise velocity, $k_x E_{\tilde{u}'\tilde{u}'}/u_\tau^2$, for LES with $N = 128$. (*b*,*c*) Show vertical profiles of single- and two-point AM correlation coefficients, $R(y; y)$ (thin solid lines, (3.3)) and $R(y; y_O)$ (thick solid lines, (3.4)), respectively, for flow over case HR. In (*a*,*b*), wall-normal elevation is scaled with channel depth, δ. In (*c*), wall-normal elevation is scaled with LES filter width, Δ. Blue and black lines correspond with $N = 96$ and $N = 128$, respectively. In (*a*,*b*), solid vertical orange line corresponds to the (approximate) elevation of the roughness element height, $y_0/h = 0.1$ (Garratt 1994) (see also (2.4)), dashed vertical orange line denotes $2h/\delta \approx y_{RSL}/\delta$ (dictated by (2.4)), and vertical solid black line denotes reference elevation, y_O/δ (see table 1). In (*a*), solid horizontal blue lines at scales of interest are shown (with annotations), and the horizontal orange line at $\lambda_x/\delta = 1$ is shown since it is the filter scale in the present AM decomposition (see § 1.1). In (*b*), black squares denote smooth-wall channel flow $R(y; y)$, taken from (Mathis *et al.* 2009*b*) (their figure 3*a*), and grey shading is added to highlight the logarithmic region.

Figure 5(*a*) shows a contour of premultiplied spectral density of resolved (LES) streamwise fluctuating velocity, $k_x E_{\tilde{u}'\tilde{u}'}/u_\tau^2$, where $k_x = 2\pi/\lambda_x$ is wavenumber and λ_x is wavelength (Hutchins & Marusic 2007*b*). Here, λ_x is recovered from the time series with Taylor's hypothesis via selection of a convection velocity, U_c. In this study, we selected $U_c = U_0$. Mathis *et al.* (2009*a*) considered U_c effects on premultiplied spectral density contours and correlation between $\tilde{u}'_L(y, t)$ and $E_L(\tilde{u}'_S(y, t))$, $R(y; y)$ (discussion to follow). They reported that changing U_c 'shifts' the distribution of $k_x E_{\tilde{u}'\tilde{u}'}/u_\tau^2$ across λ_x, but that a robust scale separation remains and, importantly, that $\lambda_x/\delta = 1$ is clearly between the wavelengths corresponding with the inner and outer peaks in energy content. They also demonstrated that U_c has a relatively modest impact on the resulting $R(y; y)$ profile. The figure 5(*a*) contour demonstrates a clear outer peak across $2 \lesssim \lambda_x/\delta \lesssim 5$ and $y/\delta \approx 0.16$, which is consistent with the

https://doi.org/10.1017/jfm.2015.744 Published online by Cambridge University Press

signature of large-scale motions (LSMs, Hutchins & Marusic 2007*a*; Mathis *et al.* 2009*a*; Fang & Porté-Agel 2015). Note, however, that the present computational domain does not capture content associated with very-large-scale motions (VLSMs, or so-called 'superstructures', Hutchins & Marusic 2007*a*; Fang & Porté-Agel 2015). Thus, we do not resolve the plateau and 'second peak' at $\lambda_x/\delta \approx 20$ due to VLSMs which occur at these asymptotic Reynolds number conditions (Fang & Porté-Agel 2015). In this work, we argue that LSMs – which are resolved in the domain – represent the 'building blocks' of VLSMs (in accordance with the literature from Kim & Adrian 1999; Balakumar & Adrian 2007; Dennis & Nickels 2011*a*,*b*; Ahn *et al.* 2015; Hellström, Ganapathisubramania & Smits 2015). Thus, since LSMs are resolved, they embody the physics imparted by VLSMs since the latter form via quasistreamwise coalescence of the former. With this, we select $\lambda_x/\delta = 1$ as a separating scale for the present rough-wall LES, since scales exceeding λ_x/δ will be related to LSMs and application of the AM decoupling procedure will therefore reveal their effect on sub-δ motions. For illustration, we added the LES grid-filter width, Δ/δ, to figure 5(*a*) ($\Delta = (\Delta_x\Delta_y\Delta_z)^{1/3}$, Deardorff 1974; Scotti, Meneveau & Lilly 1993; Bou-Zeid *et al.* 2005), which demonstrates the spatial scales resolved on the LES mesh. The figure 5(*a*) spectral density provides a guide for selecting the reference elevation, which we chose here as $y_O/\delta = 0.16$. Thus, we can identify AM of $\tilde{u}'_S(y, t)$ by $\tilde{u}'_L(y_O, t + \delta\tau(y_O; y))$, where y_O captures large-scale energy-containing structures (please see continuing discussion below).

To determine the 'strength' of the AM effect, we follow the Mathis *et al.* (2009*a*) approach by determining the correlation between $E_L(\tilde{u}'_S(y, t))$ and the large-scale signal. We can compute correlations based on single-point:

$$R(y; y) = \frac{\langle \tilde{u}'_L(y, t) E_L(\tilde{u}'_S(y, t))\rangle_T}{\langle \tilde{u}'^2_L(y, t)\rangle_T^{1/2} \langle E_L^2(\tilde{u}'_S(y, t))\rangle_T^{1/2}} \tag{3.3}$$

or two-point measurements:

$$R(y; y_O) = \frac{\langle \tilde{u}'_L(y_O, t + \delta\tau(y; y_O)) E_L(\tilde{u}'_S(y, t))\rangle_T}{\langle \tilde{u}'^2_L(y_O, t + \delta\tau(y; y_O))\rangle_T^{1/2} \langle E_L^2(\tilde{u}'_S(y, t))\rangle_T^{1/2}}. \tag{3.4}$$

Thus, (3.4) can be used to determine AM of $\tilde{u}'_S(y_i, t)$ by $\tilde{u}'_L(y_O, t + \delta\tau(y_i; y_O))$. Please see (3.2) and accompanying discussion for elaboration about the advective correction, $\delta\tau(y; y_O)$, which is essential to account for the time delay between passage of inclined coherent structures in the outer layer and their 'footprint' in the roughness sublayer (Piomelli *et al.* 1989; Marusic *et al.* 2001; Coceal *et al.* 2007; Marusic & Heuer 2007; Mathis *et al.* 2009*a*; Wu & Christensen 2010; Anderson *et al.* 2015). Table 1 summarizes the reference elevations with respect to channel depth and roughness element scale; in all cases, y_O has been carefully selected to ensure that correlations are evaluated with respect to inertial layer flow processes (i.e. $y_O/h > 2$ or $y_O/y_{RSL} > 1$). And, although $2 \lesssim y_{RSL}/h \lesssim 5$ (Grass 1971; Raupach *et al.* 1991; Mejia-Alvarez & Christensen 2010) is the widely accepted range for y_{RSL}, we note also that for the present CR case (Cheng & Castro 2002), local mean streamwise velocity profiles all converge to a plane-averaged value for $y/h \lesssim 2$ (Coceal *et al.* 2007; Anderson *et al.* 2015).

Figure 5(*b*,*c*) shows profiles of $R(y; y)$ and $R(y; y_O)$ for case HR, wherein wall-normal elevation is scaled against channel depth, δ (*a*), and LES filter width, Δ (*b*), respectively. In (*a*), the $R(y; y)$ and $R(y; y_O)$ profiles are similar for $y/\delta \lesssim 0.2$,

https://doi.org/10.1017/jfm.2015.744 Published online by Cambridge University Press

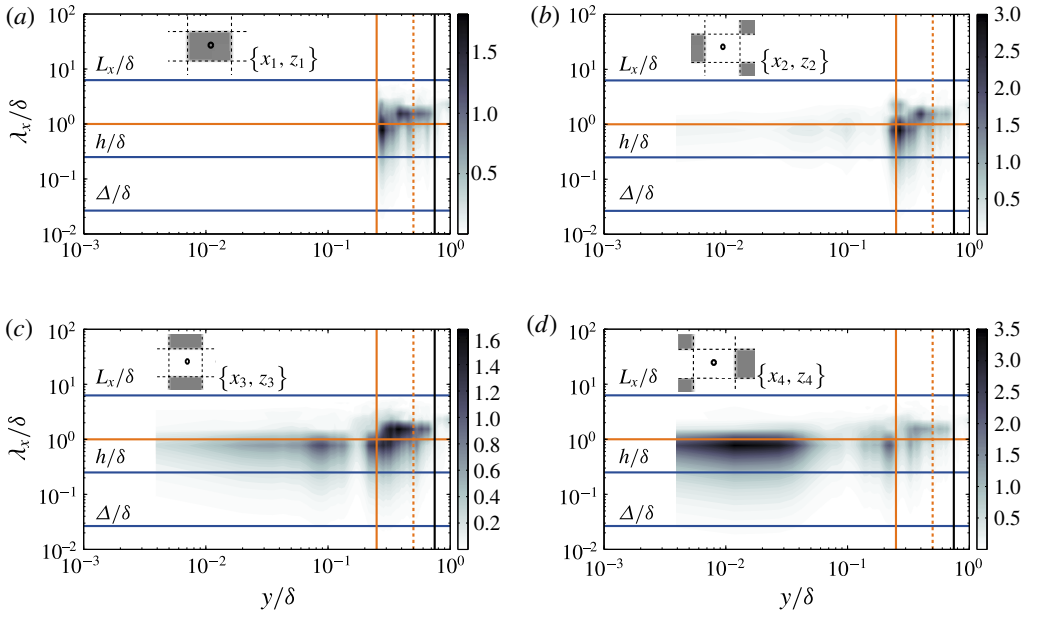


FIGURE 6. Premultiplied spectral density of streamwise velocity, $k_x E_{\tilde{u}'\tilde{u}'}/u_\tau^2$, for flow over case CR at positions indicated in figure insets. Spectral density shown here for LES with $N = 128$. Wall-normal elevation is scaled with channel depth, δ. Solid vertical orange line corresponds to the roughness element height, $h/\delta = 0.25$, dashed vertical orange line denotes $2h/\delta$, and vertical solid black line denotes reference elevation, y_O. For reference, solid horizontal blue lines at scales of interest are shown (with appropriate annotations), and the horizontal orange line at $\lambda_x/\delta = 1$ is shown since it is the filter scale in the present AM decomposition (see § 1.1).

above which the profiles diverge, with $R(y; y_O)$ declining to zero. This divergence shows that $\tilde{u}'_L(y_O, t + \delta\tau(y; y_O))$ is more weakly correlated with $E_L(\tilde{u}'_S(y, t))$ for increasing y (while, at the same elevation, $E_L(\tilde{u}'_S(y, t))$ and $\tilde{u}'_L(y, t)$ remain quite strongly correlated). For $y/\delta \lesssim 0.05$ – where the range of turbulent scales owing to shear production of turbulence is greatest and subgrid-scale stresses are maximum – both correlations are elevated. Moreover, close inspection illustrates that $R(y; y) > R(y; y_O)$ for $y/\delta \lesssim 0.05$, which is a physically meaningful outcome of correlating $E_L(\tilde{u}'_S(y, t))$ against $\tilde{u}'_L(y, t)$, instead of $\tilde{u}'_L(y_O, t + \delta\tau(y; y_O))$. Nonetheless, comparison of the rough-wall $R(y; y)$ profile against that for a smooth-wall channel (black squares, taken from Mathis *et al.* (2009*b*), their figure 3*a*) illustrates that the correlation is stronger in the presence of roughness. Note that $\delta/h \sim O(10^2)$ for the present HR case (assuming that $h/l \approx 10$, as per (2.4)), thus rendering this case a 'roughness' (Jimenez 2004; Flack & Schultz 2010; Hong *et al.* 2012) with flow statistics that will conform with Townsend's wall similarity hypothesis (Townsend 1976; Wu & Christensen 2007, 2010). One of course expects this since the roughness sublayer is parameterized via the equilibrium logarithmic law through the roughness length, l ((2.2) and (2.3)). It is therefore interesting that $R(y; y)$ and $R(y; y_O)$ in the roughness sublayer and outer (inertial) layer exceed the smooth-wall values.

Figure 6 shows $k_x E_{\tilde{u}'\tilde{u}'}/u_\tau^2$ contours for flow over case CR (figure insets illustrate spatial position). We again have included horizontal lines at reference scales

https://doi.org/10.1017/jfm.2015.744 Published online by Cambridge University Press

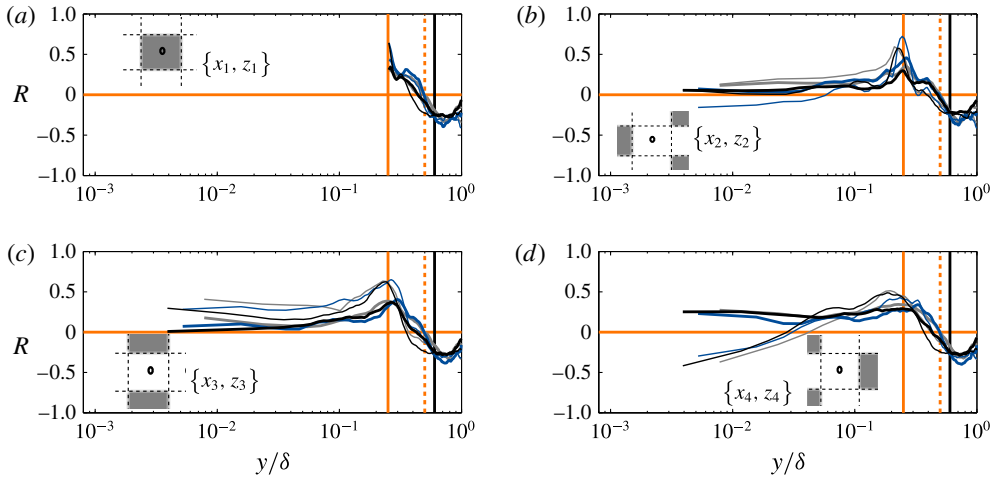


FIGURE 7. Vertical profiles of single- and two-point AM correlation coefficients, $R(y;\, y)$ (thin solid lines, (3.3)) and $R(y;\, y_O)$ (thick solid lines, (3.4)), respectively, for flow over case CR. Wall-normal elevation is scaled with channel depth, δ. Grey, blue, and black lines correspond with $N = 64$, $N = 96$, and $N = 128$, respectively. Solid vertical orange line corresponds to the roughness element height, $h/\delta = 0.25$, dashed vertical orange line denotes $2h/\delta$, and vertical solid black line denotes reference elevation, y_O.

(Δ/δ, h/δ, and L_x/δ), which provide perspective on energy content at different scales as it relates to wall-normal elevation. At $\{x_1,\, z_1\}$, there is no data for $y/\delta \leqslant h/\delta$ (owing to the 'immersed points'). Immediately above this, however, for $5 \times 10^{-1} \lesssim \lambda_x/\delta \lesssim 1.2 \times 10^0$, $k_x E_{\tilde{u}'\tilde{u}'}/u_\tau^2$ exhibits a peak that is associated with production of turbulence from the roughness element. At downwind positions, this peak remains but occurs at lower elevations, which is due to the shearing layer present at the approximate cube height. At $\{x_1,\, z_1\}$, there is also a second peak located at $\lambda_x/\delta \approx 1.8 \times 10^0$, for $0.3 \leqslant y/\delta \leqslant 0.7$, which indicates the presence of large structures (scale exceeding δ) in the domain. In fact, energy content at this wavelength and elevation is present at all locations (see figure 6*b–d*), and this has guided our selection of $y_O/\delta = 0.6$ (i.e. $y_O/y_{RSL} > 1$, and $\tilde{u}'_L(y_O, t + \delta\tau(y; y_O))$ contains significant large-scale energy content). In DNS studies of flow over case CR, Coceal *et al.* (2007) have shown that vertical profiles of time-averaged velocity at positions $\{x_1,\, x_1\}$, $\{x_2,\, x_2\}$, $\{x_3,\, x_3\}$, and $\{x_4,\, x_4\}$ (see figure 1*b*) all merge with the plane- and time-averaged vertical profile slightly above the cubes (their figure 5*a*); in LES modelling of flow over the same arrangement, we (Anderson *et al.* 2015) also observed this trend. Thus, $y_O/\delta = 0.6$ is in the inertial (logarithmic) layer, and therefore the large scales (retrieved from low-pass filtering) are low- and high-momentum regions and it is their influence on the roughness sublayer that is of interest here. Figure 6 also contains important information on downwind evolution of turbulence below the cube heights. At $\{x_2,\, z_2\}$, there is limited content at smaller scales for $y/\delta \lesssim 0.2$. At $\{x_3,\, z_3\}$, an inner peak has emerged at $\lambda_x/\delta \approx 8 \times 10^{-1}$ for $10^{-2} \lesssim y/\delta \lesssim 1.5 \times 10^{-1}$, which appears to broaden (and lower) at $\{x_4,\, z_4\}$. As discussed below, sub-δ spectral density below the cube height has important implications for correlating $\tilde{u}'_L(y_O, t + \delta\tau(y/h < 1; y_O))$ with $\tilde{u}'_S(y/h < 1, t)$.

Figures 7 and 8 show $R(y;\, y)$ and $R(y;\, y_O)$ profiles for the CR case at spatial positions $\{x_1,\, z_1\}$, $\{x_2,\, z_2\}$, $\{x_3,\, z_3\}$, and $\{x_4,\, z_4\}$ (see figure insets). Figure 7 shows the

https://doi.org/10.1017/jfm.2015.744 Published online by Cambridge University Press

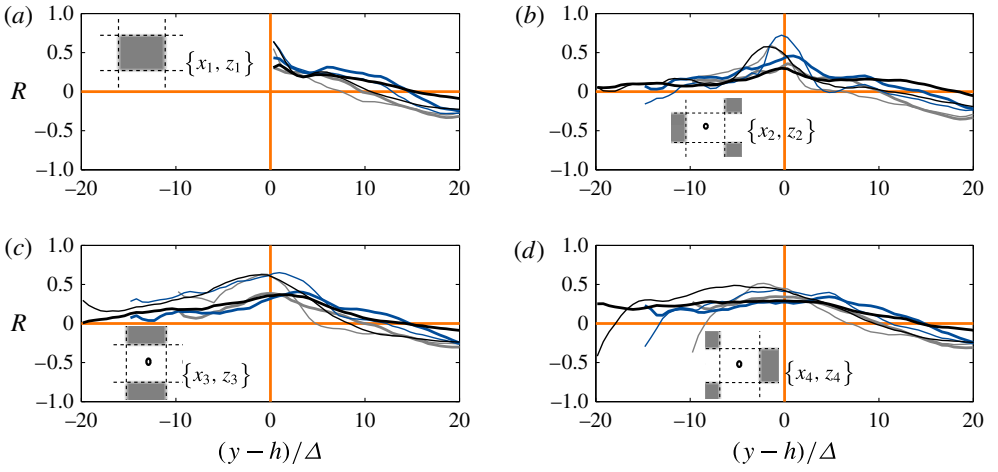


FIGURE 8. Vertical profiles of single- and two-point AM correlation coefficients, $R(y;\, y)$ (thin solid lines, (3.3)) and $R(y;\, y_O)$ (thick solid lines, (3.4)), respectively. Here, wall-normal elevation is scaled with LES filter width, Δ, which provides a means to compare across LES cases and to provide more detail on the correlation profiles in close proximity to the cube height. Grey, blue, and black lines correspond with $N = 64$, $N = 96$, and $N = 128$, respectively.

correlations against y/δ (with h/δ, y_{RSL}/δ, and y_O/δ included for reference). Since these results are from LES with an IBM that resolves the roughness sublayer, they reveal the extent to which local flow processes within the sublayer influence the correlations. Consider, for example, the profiles at positions $\{x_2,\, z_2\}$ and $\{x_3,\, z_3\}$, which demonstrate that $E_L(\tilde{u}'_S(y,\, t))$ is not correlated with $\tilde{u}'_L(y_O,\, t + \delta\tau(y;\, y_O))$ for $y/\delta \lesssim 0.1$ (or $y/h \lesssim 0.4$). At $\{x_4,\, z_4\}$, $R(y;\, y_O)$ is substantially higher below the cubes. However, at all positions, $R(y;\, y_O) \approx 0.4$ at the cube height, $y/h = 1$. It is at this height that the x–y turbulent (Reynolds) shear stresses are highest (Ghisalberti 2009), which is important in terms of modelling surface drag. In contrast, the single-point ($R(y;\, y)$) correlations are elevated at positions $\{x_2,\, z_2\}$ and $\{x_3,\, z_3\}$, and negative at $\{x_4,\, z_4\}$. At $\{x_2,\, z_2\}$ and $\{x_3,\, z_3\}$, this confirms that the small-scale content of roughness sublayer secondary flows (due to intermittent vortex shedding from cubes, recirculating flow, and downwind migration of Kelvin–Helmholtz vortices associated with 'Stuart' vortices) is positively correlated with its large-scale content (though not adequately strong to be correlated with large-scale content in the inertial layer). In contrast, $R(y;\, y) < 0$ at $\{x_4,\, z_4\}$ for $0 \leqslant y/\delta \lesssim 0.05$, which is due to mean recirculating flow upwind of the next cube. We note, however, that above the cubes (but still in the roughness sublayer, i.e. $0.25 \lesssim y/\delta \lesssim 0.5$) the correlation profiles are all relatively similar (based on single- and two-point correlation). We emphasize fundamental differences between case CR (channel flow with topography) and smooth-wall turbulent boundary layers, which were first used to demonstrate the presence of AM in wall turbulence (Marusic *et al.* 2010). Indeed, turbulence statistics for case CR will not exhibit outer-layer similarity, and thus coherent structures present for case CR may not have the spatial footprint of those present for case HR or smooth walls. Nonetheless, through application of the AM decoupling procedure (Mathis *et al.* 2009*a*), we demonstrate clear correlation between inertial and roughness sublayer processes.

https://doi.org/10.1017/jfm.2015.744 Published online by Cambridge University Press

In order to gain more insight on the roughness sublayer, we have also plotted the CR case correlation profiles against $(y-h)/\Delta$, where $\Delta = (\Delta_x \Delta_y \Delta_z)^{1/3}$ is the LES grid resolution (Deardorff 1974; Scotti *et al.* 1993; Bou-Zeid *et al.* 2005) and h represents the elevation at which the streamwise–wall-normal Reynolds (total) shearing stresses are maximum (Coceal *et al.* 2007) (although, in reality, the elevation corresponding with maximum $\widetilde{u'w'}/u_\tau^2$ exhibits spatial variation in these canopy flows, Anderson & Chamecki 2014). Normalizing by Δ is helpful in LES studies that feature resolution testing (Bou-Zeid *et al.* 2005). It is clear firstly that the LES results do not exhibit resolution dependence. Moreover, this plotting convention demonstrates generally positive correlation between $E_L(\tilde{u}'_S(y,\, t))$ and $\tilde{u}'_L(y_O,\, t+\delta\tau(y;\, y_{Ref.}))$, where the maximum values occur slightly above the cube height for positions $\{x_1,\, z_1\}$, $\{x_2,\, z_2\}$, and $\{x_3,\, z_3\}$. The large- and small-scale contents exhibit strong correlation at the same elevations ($R(y;\, y)$), with maximum values also occurring at the cube height, $(y-h)/\Delta = 0$.

4. Conclusion

The passage of coherent large-scale motions in the outer layer of smooth-wall turbulent boundary layers induces an amplitude modulation of the near-wall region of the flow (Mathis *et al.* 2009*a*,*b*; Marusic *et al.* 2010; Mathis *et al.* 2011). Mathis *et al.* (2009*a*) provided a decoupling procedure that can be used to quantify AM effects. In this study, we have presented data from LES of turbulent half-channel flow over a roughness and topography. By following the AM decoupling procedure of Mathis *et al.* (2009*a*), we have demonstrated the following.

(1) AM is present in rough-wall turbulent channel flow. For the cases considered (with $\delta/h = 4$ and $\delta/h \approx 100$), we can correlate an advective-corrected outer (inertial layer) large-scale signal, $\tilde{u}'_L(y_O,\, t+\delta\tau(y_O;\, y_i))$, with a small-scale signal in the roughness sublayer, $\tilde{u}'_S(y_i,\, t)$ (two-point correlation, $R(y_O;\, y_i)$). Alternatively, we can correlate the large- ($\tilde{u}'_L(y,\, t)$) and small-scale ($\tilde{u}'_S(y,\, t)$) signals at each elevation (single-point correlation, $R(y;\, y)$). In both approaches, we report correlation profiles comparable to those reported by Mathis *et al.* (2009*a*,*b*). For the homogeneous roughness case with $\delta/h \approx 100$, the roughness sublayer correlation is stronger than in the logarithmic region of a smooth-wall channel flow (see figure 5*b*,*c*). This is likely a manifestation of the very high (limiting) Reynolds number conditions inherent to the present simulations, wherein the logarithmic region encompasses the depth of the domain. With this, the 'inner' and 'outer' correlations are between structurally similar regions of the domain.

(2) For channel flow over the topography case, with $\delta/h = 4$, the correlations ($R(y;\, y_O)$ and $R(y;\, y)$) exhibit enormous spatial variability in the 'canopy' (i.e. $y/h < 1$; see figures 7 and 8). This spatial variability is a product of roughness sublayer secondary flows associated with individual roughness elements. Premultiplied spectral density contours were used to demonstrate that the presence of sub-δ energy content is necessary to correlate the inertial layer with processes below the element height. And, while the profiles vary greatly depending on proximity to cubes and position to upwind/downwind or adjacent cubes, the $R(y;\, y_O)$ and $R(y;\, y)$ correlations are still high. Moreover, the $R(y;\, y_O)$ and $R(y;\, y)$ profiles all converge above the canopy (in the roughness sublayer and inertial layer).

https://doi.org/10.1017/jfm.2015.744 Published online by Cambridge University Press

(3) By running a series of LES cases at different resolutions, we demonstrate grid invariance of the profiles and thus address concerns regarding grid sensitivity. Given the motivating arguments underpinning this study – documenting the existence of an AM effect in high-Re_τ LES – this result is important as it demonstrates that spatial filtering operations inherent to subgrid-scale modelling can be performed with no apparent effect on the inner–outer correlations. Though not surprising given $\delta/\Delta \gg 1$, the result confirms that the large scales exhibit an equally strong correlation with the smallest resolved scales.

In the present work, we have considered only AM of the fluctuating streamwise velocity component, although one notes more recent studies that have demonstrated AM effects in other flow statistics (Mathis *et al.* 2013; Talluru *et al.* 2014). Here, we sought only to demonstrate the presence of an AM effect in the roughness sublayer by the outer inertial layer flow. That AM exists, and that the correlations are stronger than in smooth-wall flows, is by itself relevant. On a similar note, the structure of a predictive model for the inner (near-wall) signal based on AM was originally presented by Marusic *et al.* (2010). This predictive model was thoroughly presented and tested in Mathis *et al.* (2011), wherein the authors demonstrated that empirically determined parameters – α (superposition), β (modulation), structural inclination angle, $\theta(y)$, and a universal signal, $u_*(y, t)$ – can be used in conjunction with $\tilde{u}'_L(y_O, t + \delta\tau(y_O; yi))$ to predict $\tilde{u}'_S(y_i, t)$. For brevity, we have elected here to not explore generalization of the Marusic *et al.* (2010) model for rough-wall flows. It is nonetheless promising that an AM effect can be readily identified for the present rough-wall cases (derived from LES at Reynolds numbers typical of the atmospheric surface layer or applications relevant to aerospace engineering).

Acknowledgements

This work was supported by the Air Force Office of Scientific Research (Program Manager: Dr R. Ponnappan) under grant no. FA9550-14-1-0101. Computational resources were provided by the Texas Advanced Computing Center at the University of Texas at Austin. I thank K. T. Christensen (University of Notre Dame) and anonymous reviewers for providing helpful critiques of the original manuscript. Thank you also to A. Awasthi (University of Texas at Dallas) for assistance with preparing figure 5.

REFERENCES

AHN, J., LEE, J. H., LEE, J., KANG, J.-H. & SUNG, H. J. 2015 Direct numerical simulation of a $30r$ long turbulent pipe flow at $Re_\tau = 3008$. *Phys. Fluids* **27**, 065110.

ALBERTSON, J. & PARLANGE, M. 1999 Surface length scales and shear stress: implications for land–atmosphere interaction over complex terrain. *Water Resour. Res.* **35**, 2121–2132.

ANDERSON, W. 2012 An immersed boundary method wall model for high-Reynolds number channel flow over complex topography. *Int. J. Numer. Methods Fluids* **71**, 1588–1608.

ANDERSON, W. & CHAMECKI, M. 2014 Numerical study of turbulent flow over complex aeolian dune fields: the White Sands National Monument. *Phys. Rev.* E **89**, 013005.

ANDERSON, W., LI, Q. & BOU-ZEID, E. 2015 Numerical simulation of flow over urban-like topographies and evaluation of turbulence temporal attributes. *J. Turbulence* **16**, 809–831.

ANDERSON, W. & MENEVEAU, C. 2010 A large-eddy simulation model for boundary-layer flow over surfaces with horizontally resolved but vertically unresolved roughness elements. *Boundary-Layer Meteorol.* **137**, 397–415.

https://doi.org/10.1017/jfm.2015.744 Published online by Cambridge University Press

ANDERSON, W. & MENEVEAU, C. 2011 A dynamic large-eddy simulation model for boundary layer flow over multiscale, fractal-like surfaces. *J. Fluid Mech.* **679**, 288–314.

BAI, K., MENEVEAU, C. & KATZ, J. 2012 Near-wake turbulent flow structure and mixing length downstream of a fractal-tree. *Boundary-Layer Meteorol.* **143**, 285–308.

BAILEY, B. N. & STOLL, R. 2013 Turbulence in sparse, organized vegetative canopies: a large-eddy simulation study. *Boundary-Layer Meteorol.* **147**, 369–400.

BALAKUMAR, B. J. & ADRIAN, R. J. 2007 Large- and very-large-scale motions in channel and boundary-layer flows. *Phil. Trans. R. Soc. Lond.* A **365**, 665–681.

BALARAS, E. & BENOCCI, C. 1994 Subgrid-scale models in finite-difference simulations of complex wall bounded flows. In *AGARD CP 551*. AGARD, Neuilly-sur-Seine, France, p. 2.15.

BALARAS, E., BENOCCI, C. & PIOMELLI, U. 1996 Two layer approximate boundary conditions for large-eddy simulations. *AIAA J.* **34**, 11119.

BANDYOPADHYAY, P. R. & HUSSAIN, A. K. M. F. 1984 The coupling between scales in shear flows. *Phys. Fluids* **27**, 2221–2228.

BELCHER, S. E., HARMAN, I. N. & FINNIGAN, J. J. 2012 The wind in the willows: flows in forest canopies in complex terrain. *Annu. Rev. Fluid Mech.* **44**, 479–504.

BOHM, M., FINNIGAN, J. J. & RAUPACH, M. R. 2000 Dispersive fluxes and canopy flows: just how important are they? In *Proc. 24th Conf. on Agricultural and Forest Meteorology*. American Meteorological Society, Davis, CA, pp. 106–107.

BONS, J. P., TAYLOR, R. P., MCCLAIN, S. T. & RIVIR, R. B. 2001 The many faces of turbine surface roughness. *Trans. ASME J. Turbomach.* **123**, 739–748.

BOU-ZEID, E., MENEVEAU, C. & PARLANGE, M. B. 2005 A scale-dependent Lagrangian dynamic model for large eddy simulation of complex turbulent flows. *Phys. Fluids* **17**, 025105.

CALAF, M., MENEVEAU, C. & MEYERS, J. 2010 Large eddy simulation study of fully developed wind-turbine array boundary layers. *Phys. Fluids* **22**, 015110.

CALAF, M., PARLANGE, M. B. & MENEVEAU, C. 2011 Large eddy simulation study of scalar transport in fully developed wind-turbine array boundary layers. *Phys. Fluids* **23**, 126603.

CASTRO, I. P. 2007 Rough-wall boundary layers: mean flow universality. *J. Fluid Mech.* **585**, 469–485.

CHAN, L., MACDONALD, M., CHUNG, D., HUTCHINS, N. & OOI, A. 2015 A systematic investigation of roughness height and wavelength in turbulent pipe flow in the transitionally rough regime. *J. Fluid Mech.* **771**, 743–777.

CHENG, H. & CASTRO, I. P. 2002 Near wall flow over urban-like roughness. *Boundary-Layer Meteorol.* **104**, 229–259.

CHESTER, S., MENEVEAU, C. & PARLANGE, M. B. 2007 Modelling of turbulent flow over fractal trees with renormalized numerical simulation. *J. Comput. Phys.* **225**, 427–448.

COCEAL, O., DOBRE, A., THOMAS, T. G. & BELCHER, S. E. 2007 Structure of turbulent flow over regular arrays of cubical roughness. *J. Fluid Mech.* **589**, 375–409.

DEARDORFF, J. W. 1970 A numerical study of three-dimensional turbulent channel flow at large Reynolds numbers. *J. Fluid Mech.* **41**, 453–480.

DEARDORFF, J. W. 1974 Three dimensional numerical study of turbulence in an entraining mixed layer. *Boundary-Layer Meteorol.* **7**, 199–226.

DENNIS, D. J. C. & NICKELS, T. B. 2011*a* Experimental measurement of large-scale three-dimensional structures in a turbulent boundary layer. Part 1. Vortex packets. *J. Fluid Mech.* **673**, 180–217.

DENNIS, D. J. C. & NICKELS, T. B. 2011*b* Experimental measurement of large-scale three-dimensional structures in a turbulent boundary layer. Part 2. Long structures. *J. Fluid Mech.* **673**, 218–244.

FANG, J. & PORTÉ-AGEL, F. 2015 Large-eddy simulation of very-large-scale motions in the neutrally stratified atmospheric boundary layer. *Boundary-Layer Meteorol.* **155**, 397–416.

FINNIGAN, J. 2000 Turbulence in plant canopies. *Annu. Rev. Fluid Mech.* **32**, 519–571.

FINNIGAN, J. J., SHAW, R. H. & PATTON, E. G. 2009 Turbulence structure above a vegetation canopy. *J. Fluid Mech.* **637**, 387–424.

https://doi.org/10.1017/jfm.2015.744 Published online by Cambridge University Press

FLACK, K. A. & SCHULTZ, M. P. 2010 Review of hydraulic roughness scales in the fully rough regime. *Trans. ASME J. Fluids Eng.* **132**, 041203.

GANAPATHISUBRAMANI, B., LONGMIRE, E. K. & MARUSIC, I. 2003 Characteristics of vortex packets in turbulent boundary layers. *J. Fluid Mech.* **478**, 35–46.

GARRATT, J. R. 1994 *The Atmospheric Boundary Layer*. Cambridge University Press.

GHISALBERTI, M. 2009 Obstructed shear flows: similarities across systems and scales. *J. Fluid Mech.* **641**, 51–61.

GRAHAM, J. & MENEVEAU, C. 2012 Modeling turbulent flow over fractal trees using renormalized numerical simulation: alternate formulations and numerical experiments. *Phys. Fluids* **24**, 125105.

GRASS, A. J. 1971 Structural features of turbulent flow over smooth and rough boundaries. *J. Fluid Mech.* **50**, 233–255.

HARMON, I. & FINNIGAN, J. J. 2007 A simple unified theory for flow in the canopy and roughness sublayer. *Boundary-Layer Meteorol.* **123**, 339–364.

HELLSTRÖM, L. H. O., GANAPATHISUBRAMANIA, B. & SMITS, A. J. 2015 The evolution of large-scale motions in turbulent pipe flow. *J. Fluid Mech.* **779**, 701–715.

HONG, J., KATZ, J., MENEVEAU, C. & SCHULTZ, M. 2012 Coherent structures and associated subgrid-scale energy transfer in a rough-wall channel flow. *J. Fluid Mech.* **712**, 92–128.

HONG, J., KATZ, J. & SCHULTZ, M. 2011 Near-wall turbulence statistics and flow structures over three-dimensional roughness in a turbulent channel flow. *J. Fluid Mech.* **667**, 1–37.

HUTCHINS, N. & MARUSIC, I. 2007*a* Evidence of very long meandering features in the logarithmic region of turbulent boundary layers. *J. Fluid Mech.* **579**, 1–28.

HUTCHINS, N. & MARUSIC, I. 2007*b* Large-scale influences in near-wall turbulence. *Phil. Trans. R. Soc. Lond.* A **365**, 647–664.

HUTCHINS, N., NICKELS, T. B., MARUSIC, I. & CHONG, M. S. 2009 Hot-wire spatial resolution issues in wall-bounded turbulence. *J. Fluid Mech.* **635**, 103–136.

JIMENEZ, J. 2004 Turbulent flow over rough wall. *Annu. Rev. Fluid Mech.* **36**, 173–196.

KIM, K. C. & ADRIAN, R. J. 1999 Very large-scale motion in the outer layer. *Phys. Fluids* **11**, 417–422.

KROGSTAD, P.-A. & ANTONIA, R. A. 1994 Structure of turbulent boundary layers on smooth and rough walls. *J. Fluid Mech.* **277**, 1–21.

LEONARDI, S. & CASTRO, I. P. 2010 Channel flow over large cube roughness: a direct numerical simulation study. *J. Fluid Mech.* **651**, 519–539.

LEONARDI, S., ORLANDI, P. & ANTONIA, R. A. 2007 Properties of *d*- and *k*-type roughness in a turbulent channel flow. *Phys. Fluids* **19**, 125101.

LEONARDI, S., ORLANDI, P., SMALLEY, R. J., DJENIDI, L. & ANTONIA, R. A. 2003 Direct numerical simulations of turbulent channel flow with transverse square bars on one wall. *J. Fluid Mech.* **491**, 229–238.

LUNDQUIST, K. A., CHOW, F. K. & LUNDQUIST, J. K. 2010 An immersed boundary method for the weather research and forecasting model. *Mon. Weather Rev.* **138**, 796–817.

MARUSIC, I. & HEUER, W. D. C. 2007 Reynolds number invariance of the structure angle in wall turbulence. *Phys. Rev. Lett.* **99**, 114501.

MARUSIC, I., KUNKEL, G. J. & PORTÉ-AGEL, F. 2001 Experimental study of wall boundary conditions for large-eddy simulation. *J. Fluid Mech.* **446**, 309–320.

MARUSIC, I., MATHIS, R. & HUTCHINS, N. 2010 Predictive model for wall-bounded turbulent flow. *Science* **329**, 193–196.

MASON, P. J. 1994 Large-eddy simulation: a critical review of the technique. *Q. J. R. Meteorol. Soc.* **120**, 1–26.

MATHIS, R., HUTCHINS, N. & MARUSIC, I. 2009*a* Large-scale amplitude modulation of the small-scale structures in turbulent boundary layers. *J. Fluid Mech.* **628**, 311–337.

MATHIS, R., HUTCHINS, N. & MARUSIC, I. 2011 A predictive inner–outer model for streamwise turbulence statistics in wall-bounded flows. *J. Fluid Mech.* **681**, 537–566.

https://doi.org/10.1017/jfm.2015.744 Published online by Cambridge University Press

MATHIS, R., MARUSIC, I., CHERNYSHENKO, S. I. & HUTCHINS, N. 2013 Estimating wall-shear-stress fluctuations given an outer region input. *J. Fluid Mech.* **715**, 163–180.

MATHIS, R., MONTY, J. P., HUTCHINS, N. & MARUSIC, I. 2009*b* Comparison of large-scale amplitude modulation in turbulent boundary layers, pipes, and channel flows. *Phys. Fluids* **21**, 111703.

MEJIA-ALVAREZ, R. & CHRISTENSEN, K. T. 2010 Low-order representations of irregular surface roughness and their impact on a turbulent boundary layer. *Phys. Fluids* **22**, 015106.

MENEVEAU, C. & KATZ, J. 2000 Scale-invariance and turbulence models for large-eddy simulation. *Annu. Rev. Fluid Mech.* **32**, 1–32.

MITTAL, R. & IACCARINO, G. 2005 Immersed boundary methods. *Annu. Rev. Fluid Mech.* **37**, 239–261.

MOENG, C.-H. 1984 A large-eddy-simulation model for the study of planetary boundary-layer turbulence. *J. Atmos. Sci.* **41**, 2052–2062.

NADEEM, M., LEE, J. H., LEE, J. & SUNG, H. J. 2015 Turbulent boundary layers over sparsely-spaced rod-roughened walls. *Int. J. Heat Fluid Flow* **56**, 16–27.

PIOMELLI, U. 2008 Wall-layer models for large-eddy simulations. *Prog. Aerosp. Sci.* **44**, 437–446.

PIOMELLI, U. & BALARAS, E. 2002 Wall-layer models for large-eddy simulation. *Annu. Rev. Fluid Mech.* **34**, 349–374.

PIOMELLI, U., FERZIGER, J., MOIN, P. & KIM, J. 1989 New approximate boundary conditions for large eddy simulations of wall-bounded flows. *Phys. Fluids* A **1**, 1061.

POPE, S. 2000 *Turbulent Flows*. Cambridge University Press.

PORTÉ-AGEL, F., MENEVEAU, C. & PARLANGE, M. B. 2000 A scale-dependent dynamic model for large-eddy simulation: application to a neutral atmospheric boundary layer. *J. Fluid Mech.* **415**, 261–284.

RAO, K. N., NARASIMHA, R. & NARAYANAN, M. A. B. 1971 The bursting phenomena in a turbulent boundary layer. *J. Fluid Mech.* **48**, 339–352.

RAUPACH, M. R., ANTONIA, R. A. & RAJAGOPALAN, S. 1991 Rough-wall turbulent boundary layers. *Appl. Mech. Rev.* **44**, 1–25.

SAGAUT, P. 2002 *Large Eddy Simulation for Incompressible Flows*. Springer.

SCHULTZ, M. P. 2007 Effects of coating roughness and biofouling on ship resistance and powering. *Biofouling* **23**, 331–341.

SCOTTI, A., MENEVEAU, C. & LILLY, D. K. 1993 Generalized Smagorinsky model for anisotropic grids. *Phys. Fluids* **5**, 2306–2308.

SMAGORINSKY, J. S. 1963 General circulation experiments with the primitive equations. *Mon. Weather Rev.* **91**, 99–164.

STEVENS, R. J. A. M., WILCZEK, M. & MENEVEAU, C. 2014 Large-eddy simulation study of the logarithmic law for second- and higher-order moments in turbulent wall-bounded flow. *J. Fluid Mech.* **757**, 888–907.

TALLURU, K. M., BAIDYA, R., HUTCHINS, N. & MARUSIC, I. 2014 Amplitude modulation of all three velocity components in turbulent boundary layers. *J. Fluid Mech.* **746**, R1,1–11.

TOWNSEND, A. A. 1976 *The Structure of Turbulent Shear Flow*. Cambridge University Press.

TSENG, Y.-H., MENEVEAU, C. & PARLANGE, M. B. 2006 Modeling flow around bluff bodies and predicting urban dispersion using large-eddy simulation. *Environ. Sci. Technol.* **40**, 2653–2662.

VOLINO, R. J., SCHULTZ, M. P. & FLACK, K. A. 2007 Turbulence structure in rough- and smooth-wall boundary layers. *J. Fluid Mech.* **592**, 263–293.

WILCZEK, M., STEVENS, R. J. A. M. & MENEVEAU, C. 2015 Spatio-temporal spectra in the logarithmic layer of wall turbulence: large-eddy simulations and simple models. *J. Fluid Mech.* **769**, R1.

WU, Y. & CHRISTENSEN, K. T. 2007 Outer-layer similarity in the presence of a practical rough-wall topology. *Phys. Fluids* **19**, 085108.

WU, Y. & CHRISTENSEN, K. T. 2010 Spatial structure of a turbulent boundary layer with irregular surface roughness. *J. Fluid Mech.* **655**, 380–418.

https://doi.org/10.1017/jfm.2015.744 Published online by Cambridge University Press

XIE, Z.-T., COCEAL, O. & CASTRO, I. P. 2008 Large-eddy simulation of flows over random urban-like obstacles. *Boundary-Layer Meteorol.* **129**, 1–23.

YANG, X. I. A., SADIQUE, J., MITTAL, R. & MENEVEAU, C. 2015 Integral wall model for large eddy simulations of wall-bounded turbulent flows. *Phys. Fluids* **27**, 025112.

YUAN, J. & PIOMELLI, U. 2014 Roughness effects on the Reynolds stress budgets in near-wall turbulence. *J. Fluid Mech.* **760**, R1.

https://doi.org/10.1017/jfm.2015.744 Published online by Cambridge University Press